



Functionalization of expanded MXene to recover palladium ions by capacitive deionization

Jiming Lu^{a,b,c,1}, Shuangzhe Zhang^{a,d,1}, Chuan Zhou^a, Xinyang Wang^{a,b}, Binda Lu^{a,b}, Yi Liu^{a,b}, Yingzhi Li^{a,b}, Timothy N. Hunter^c, Zhouguang Lu^{a,b}, Lei Li^{a,*}, David Harbottle^{c,*}, Zhenghe Xu^{a,b,*}

^a Department of Materials Science & Engineering, Southern University of Science and Technology, Shenzhen 518055, Guangdong, PR China

^b Key University, Laboratory of Highly Efficient Utilization of Solar Energy and Sustainable Development of Guangdong, Southern University of Science and Technology, Shenzhen 518055, China

^c School of Chemical and Process Engineering, University of Leeds, Leeds LS2 9JT, UK

^d School of Materials Science and Engineering, Harbin Institute of Technology, Harbin 150001, China

ARTICLE INFO

Keywords:

Palladium recovery
MXene
Capacitive deionization
Sulfur doping
Nitrogen doping

ABSTRACT

This work prepared a sulfur/nitrogen co-doped MXene (S/N-MXene) electrode material via a facile hydrothermal method. The electrode material has been specifically designed to recover palladium(II) from wastewater. Numerous S/N-containing functional groups were introduced into the MXene by S and N co-doping, with the contents optimized for the preferential recovery of Pd(II). These functional groups acted as pillars to expand the interlayer spacing of MXene, facilitating Pd²⁺ diffusion between MXene layers and enhancing accessibility to the anchor sites (-OH groups and heteroatom functional groups). The S/N-MXene electrode exhibited a high recovery capacity of 2.92 mmol g⁻¹, high recovery efficiency of 96.4 % in 15 min and good long-term cycling performance with greater than 80 % capacity retained after 260 cycles. The S/N-MXene electrode showed preferential adsorption of Pd²⁺ from wastewater. The adsorption mechanism was elucidated through density functional theory (DFT) calculations showing that the downward shift of the *p*-band center of the MXene-OH groups induced by pyrrolic-N and -C=S in S/N-MXene (compared to single doping with S or N) favours enhancement of the soft ion-soft ion interactions. Furthermore, the adsorbed Pd²⁺ on the S/N-MXene electrode could be enriched by simple reversing of the applied voltage to strip the ions from the sorbent, thus avoiding the need to use harsh chemicals for regeneration and minimizing the amount of secondary waste.

1. Introduction

Due to its versatile physicochemical properties, palladium has found applications in medicine, electronics and catalysis [1,2]. Its excellent catalytic properties means that the material is abundantly used across sectors, which has unfortunately led to unintended environmental pollution [3]. Palladium pollution can come from direct (industrial effluent) and indirect (emissions from use) routes, but without technologies to remove palladium from the environment, its accumulation is a cause for concern.

Several processes have demonstrated the recovery of Pd(II) from wastewater such as solvent extraction [4], precipitation [5] and adsorption [6,7]. However, these processes often suffer from one or

multiple compromises in their performance which can be attributed to for example: the use of secondary chemicals which adds cost and potentially leads to secondary pollution; small operational window within which performance is acceptable; often slow adsorption kinetics limiting treat rates [8]; and in the case of adsorption, often single use of the adsorbent which may be reused if harsh chemical treatment is applied to the adsorbent [9].

Capacitive deionization (CDI) is seen as a potential technology that is more versatile and can address many of the limitations of existing treatment strategies [9–11]. In the CDI process, target ions are captured by the electrodes within the electric double layer (EDL) when an external direct voltage is applied between oppositely polarized electrodes [10,11]. The electrode material is vital to the performance of CDI

* Corresponding authors.

E-mail addresses: lil33@sustech.edu.cn (L. Li), d.harbottle@leeds.ac.uk (D. Harbottle), xuzh@sustech.edu.cn (Z. Xu).

¹ These authors are equally first authors.

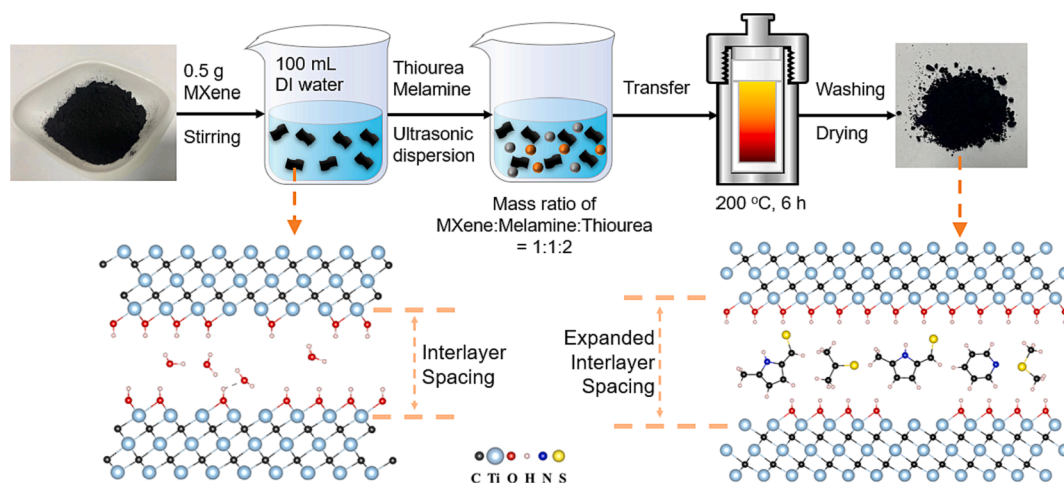


Fig. 1. The sequence of steps to prepare S/N-MXene powder used to form the CDI electrode. The chemical structures of MXene and S/N-MXene show the expanded interlayer after chemical doping.

as it transfers the electric current and forms the framework for the sorption surface, which affects adsorption capacity, kinetics, regenerability and ion selectivity. An excellent CDI electrode should exhibit good conductivity, low fouling potential, high electro-adsorption capacity and good electrochemical stability [9,11]. Various materials have been studied for CDI applications in desalination, water softening and heavy metal ion removal, including amorphous carbon [9,12], carbon nanotubes [13,14], graphene [15,16], MOF [17,18], and metal oxide [19]. However, the large-scale applications of these materials are hindered by insufficient removal capacity, high costs and complicated preparation methods [11].

Recently, MXene has attracted great interest as a promising CDI electrode material for aqueous detoxification and desalination [20–22]. MXene is a family of 2D transition metal carbides or nitrides derived from the corresponding MAX phase, wherein M is the transition metal (such as Ti, Mo, V, Cr), A and X represent the Al metallic bond layer and the carbon or nitrogen atoms, respectively. With its hydrophilic behavior, tunable chemistry and abundant functional groups on its surface, MXene has been considered as an adsorbent for the removal and recovery of Pb^{2+} [23,24], Cr(VI) [25], Cs^+ [26,27] and U(VI) [28].

Mu et al. [29] was the first to use titanium carbides as an adsorbent to recover Pd^{2+} . The authors adjusted the etching temperature during the transformation from the MAX phase to MXene to expand the layer spacing for optimal recovery with a capacity of 184.56 mg g^{-1} . However, the approach to regenerate the adsorbent used strong chemical agents to strip the Pd-ions which was complicated and produced secondary waste.

Surface functionalization using specific chemistries has been demonstrated as a method to enhance the adsorption capacity and selectivity for target ions [11,30]. Nitrogen and sulfur-containing groups are often added as they provide free non-bonding electrons that can act as a Lewis base for the preferential ion binding [11,30,31]. In addition, heteroatoms doping has been demonstrated to expand the interlayer spacing of layered materials, contributing to greater surface area and faster ionic diffusion [32,33].

In the current study, N and S co-doped carbon-coated MXene (S/N-MXene) has been successfully synthesized via a facile hydrothermal method (Fig. 1) as an electrode material for the selective recovery of Pd-ions. The synergistic effect of N and S co-doping endows MXene surface with higher contents of functional groups for the selective adsorption of Pd^{2+} , especially via pyrrolic-N, $-\text{C}=\text{S}$ and $-\text{OH}$ groups. The excellent adsorption capacity, fast kinetics, improved selectivity and long-term cycling performance enable S/N-MXene to be a highly efficient, green and regenerable CDI electrode for the selective recovery of Pd(II) from industrial wastewater.

2. Materials and methods

Synthesis of MXene: Ti_3AlC_2 (99 %, 400 mesh, Ningbojinlei) was etched by aqueous HF solution (48 %, Aladdin) at a solid-to-liquid mass ratio of 1:10 under gentle stirring at 60°C for 12 hr. The suspension was centrifuged and vacuum filtered to leave a black cake that was washed using deionized water until the filtrate was pH 7, before drying at 60°C in a vacuum oven for 12 hr.

Preparation of doped-MXene: The process to prepare S/N-MXene is shown in Fig. 1. First, 0.5 g of MXene was dispersed in 100 mL deionized water by magnetic stirring to form a homogeneous suspension. Thiourea and melamine were then dissolved into the suspension using ultrasonication; the MXene-to-melamine-to-thiourea mass ratio was 1:1:2. After that, the suspension was transferred to a 100 mL Teflon-lined autoclave and heated to 200°C for 6 hr using a ramp rate of $5^\circ\text{C}/\text{min}$ but naturally cooled to room temperature. The reacted suspension was washed with deionized water and vacuum filtered to remove any residual reactants before finally drying in a vacuum oven at 80°C for 24 hr. For comparison, nitrogen-doped MXene (N-MXene) and sulfur-doped MXene (S-MXene) were also prepared by using only melamine or thiourea following the same method but for N-MXene the mass ratio of MXene to melamine is 1:1 and for S-MXene the mass ratio of MXene to thiourea is 1:2.

Scanning electron microscope: A TM3030Plus scanning electron microscope (SEM) (Hitachi) with energy dispersive X-ray spectroscopy (EDX, Oxford Instruments, X-stream-2) was used to determine the morphology and elemental composition of each sample. The acceleration voltage was set at 10 kV with a working distance of 8 mm. Samples were dispersed in ethanol by ultrasonication and one drop of the suspension was placed onto a single-crystal silicon wafer and dried under an infrared lamp for 30 min.

Transmission electron microscope: High-resolution transmission electron microscopy (HR-TEM) images of the prepared samples were collected using an FEI Titan Themis Cubed 300 microscope (Thermo Fisher Scientific) operated at 300 kV acceleration voltage. The samples were dispersed in ethanol via ultrasonication for 15 min and one drop of the suspension was then deposited onto a copper grid of an amorphous carbon film (Beijing Zhongjingkeyi Technology Co., Ltd.) and dried under an infrared lamp for 30 min.

Nitrogen adsorption/desorption analysis: A TriStar 3000 analyzer (Micrometrics, UK) was used to measure the nitrogen adsorption/desorption isotherms of samples degassed at 200°C for 6 hr. The specific surface area of each sample was calculated by the Brunauer–Emmett–Teller (BET) method.

Fourier transform infrared spectroscopy: Fourier transform

infrared spectroscopy (FTIR) was used to determine the chemistry of MXene and doped MXene. The samples were mixed with KBr by strong vibration and the mixture was pressed into a 10 μm thick pellet. A Nicolet iS10 FT-IR spectrometer equipped with a deuterated triglycine sulphate (DTGS) KBr detector was used to obtain the FTIR spectra.

X-ray photoelectron spectroscopy: X-ray photoelectron spectroscopy (XPS) spectra were collected using a VG Multilab 2000 apparatus with a monochromated Al K-alpha X-ray source of 1486.6 eV (Thermo Fisher, Escalab 250Xi, USA). Charge build-up on the sample during the measurement was compensated by an electron/ion gun. Samples were coated on Cu conductive adhesive and placed in vacuum chamber (pressure < 10^{-7} Pa). All spectra were calibrated against the C 1 s peak (285 eV) and deconvoluted by the Avantage software using Powell fitting algorithm with Gauss-Lorentz mix product and 0.0001 convergence value.

Electrode preparation and ion adsorption: The CDI electrode was prepared by milling the active material, super P (Kejing Ltd.) and polyvinylidene fluoride (PVDF, Sigma Aldrich) at a mass ratio of 8:1:1 in N-methyl-pyrrolidone (NMP) in an agate mortar for 1 hr. The prepared slurry was then coated onto a 50- μm thick graphite paper (Jilong Special carbon) using a film applicator machine (MSK-AFA-ES200, Kejing Ltd.) with a gap spacing of 100 μm and a coater speed of 3 mm/s. The electrode was dried in a vacuum oven at 80 $^{\circ}\text{C}$ for 12 hr and cooled naturally to room temperature. Finally, the electrode was cut into a square of 80 \times 80 mm so that each electrode had 200 mg of active material.

The electrode materials were tested using a continuous CDI system which included a custom-built CDI cell, direct power source (RXN-605D, Zhaoxin), peristaltic pump (BT100-2 J, Lange), conductivity meter (Type 308A, Leici Company), feed and discharge beakers. For each CDI test, 200 mL of feed solution was cycled around the CDI system at flow rate of 20 mL/min while applying a direct voltage of either 0 V (open circuit) or 1.2 V (closed circuit). 1.2 V was chosen for the studies as the voltage-dependent adsorption capacity plateaued beyond this voltage, see Fig. S1 of the Supporting Information. The CDI system operated with an asymmetric electrode configuration of a working electrode (containing the active material) and counter electrode (graphite paper, Jilong Special Carbon) separated by a 1 mm thick silicon rubber seal. The initial concentration of Pd^{2+} in aqueous solution was varied from 0.2 to 3.0 mmol/L at pH = 6.0 \pm 0.1. At this condition, Liu et al. [34,35] reported that Pd is predominantly in the form of hydrated complexes, with $[\text{Pd}(\text{H}_2\text{O})_4]^{2+}$ being the major species and $[\text{Pd}(\text{NO}_3)(\text{H}_2\text{O}_3)]^+$ the minor species. Following each test, the equilibrium concentration was measured by atomic absorption spectrophotometry (AAS, 200 Series AA, Agilent Technologies) and the adsorption capacity of the active material determined by:

$$q = \frac{(C_0 - C_e)V}{m} \quad (1)$$

where C_0 and C_e (mmol/L) represent the initial and equilibrium ion concentrations, V (L) and m (g) are the solution volume and the mass of active material (not including the mass of binder and conductive agent) incorporated into the electrode, respectively.

The adsorption isotherm data at 0 V was fitted using the Langmuir adsorption model [11]:

$$Q_e = \frac{Q_0 K_L C_e}{1 + K_L C_e} \quad (2)$$

with the fitting parameters determined by transforming Eq. (2) into its linear form:

$$\frac{1}{Q_e} = \frac{1}{Q_0} + \frac{1}{Q_0 K_L C_e} \quad (3)$$

where Q_e and Q_0 (mmol/g) are the equilibrium and theoretical maximum capacities of the adsorbent, respectively, K_L (L/mmol) is the Langmuir constant related to the affinity coefficient of the binding sites,

and C_e (mmol/L) is the equilibrium solution concentration. The data at 1.2 V was not fitted using the Langmuir adsorption model due to the effect of an expanded EDL in the electrical field.

Electrochemical performance: Electrochemical testing of the as-prepared electrodes was performed using a CHI 604E electrochemical workstation (CH Instruments, Inc, China) with a three-electrode setup which included a working electrode, a Pt mesh counter electrode and an Ag/AgCl reference electrode. The test solution was 0.5 mmol/L Pd^{2+} . For cyclic voltammetry (CV), the voltage was varied between 0 and 1.2 V at a scan rate of 20 mV s^{-1} . Electrical impedance spectroscopy (EIS) was conducted in the frequency range of 0.01 Hz to 100 kHz with an alternating current (AC) amplitude of 5 mV. Galvanostatic charge-discharge (GCD) measurements were performed between 0 and 1 V at a current density of 0.5 A/g. The specific capacitances of MXene, S-MXene, N-MXene and S/N-MXene were determined from the GCD curves using, $C = I \times \Delta t / \Delta V$, where I , Δt , and ΔV represent the current density (A/g), discharge time (s), and voltage change (V) during the discharge process.

Adsorption kinetics: Using the CDI system the electrodes were tested at 0 V and 1.2 V with 0.5 mmol/L (C_0 – initial concentration) Pd^{2+} solution being cycled through the CDI electrode for 30 min at a flow rate of 20 mL/min (pH = 6). The concentration (C_t – time dependent concentration) of Pd^{2+} in the 200 mL test solution was measured (using AAS) at 5, 15, 30, 45, 60, 90 and 120 min. The adsorption kinetic data is fitted using the pseudo-second order rate equation (PSORE) [11]:

$$\frac{t}{Q_t} = \frac{1}{k_2 Q_e^2} + \frac{t}{Q_e} \quad (4)$$

where Q_t (mmol/g) is the adsorbed Pd^{2+} quantity at time t and k_2 ($\text{g mg}^{-1} \text{min}^{-1}$) is the sorption rate constant.

Competitive adsorption: Test fluids with competing ions (Na^+ , Ca^{2+} , K^+ , Mg^{2+} and Al^{3+}) were prepared so that each competing ion was 20 mmol/L and the concentration of Pd^{2+} was 0.5 mmol/L. With the CDI voltage set to 1.2 V the test fluid ($v = 100$ mL) was pumped through the CDI cell at a flowrate of 0.8 mL/min for 125 min. Compared to the adsorption tests, a lower flowrate was used because of the single-pass treatment of the effluent which mimics the industrial application of the CDI technique [36–38]. Furthermore, the effect of HNO_3 concentration on the CDI performance of the as-prepared materials was studied. 100 mL of effluent with 0.5 mmol/L Pd^{2+} (fixed concentration of the target ion) and varying concentrations of HNO_3 from 0 to 3 mol/L was flowed through the CDI setup at 0.8 mL/min with the voltage fixed at 1.2 V. The residual ions concentrations in the fluid effluent were measured by AAS.

Electrode durability: The regenerability of the S/N-MXene electrode was assessed by cycling the applied voltage between 1.2 V (adsorption) and -1.2 V (desorption). A 0.5 mmol/L Pd^{2+} test solution was cycled through the CDI system for 30 min at a flow rate 20 mL/min. For each adsorption and desorption step the external voltage was kept constant for 30 min (1 hr per cycle). After each 10 cycles the test solution was sampled to measure the mass of Pd^{2+} adsorbed by the electrode (q_x). The capacity retention was calculated by q_x/q_{1st} , where q_x is the adsorption capacity at x cycles, and q_{1st} is the adsorption capacity after the first cycle.

Pd^{2+} enrichment tests were conducted using the setup shown in Fig. 7c inset. The feed tank values were opened to cycle 500 mL of 0.5 mmol/L Pd^{2+} around the CDI system at 20 mL/min for 30 min while the CDI voltage was fixed at 1.2 V. Then the values were switched to the enrichment tank so the Pd^{2+} ions could be desorbed into 50 mL of deionized water as the fluid was cycled around the CDI system with the CDI voltage at -1.2 V for 30 min. The process was repeated 30 times and each time a fresh feed solution was used to ensure that the performance was not limited by depleting Pd^{2+} .

Density-functional theory simulations: All DFT spin-polarization calculations were performed with Vienna Ab-initio Simulation

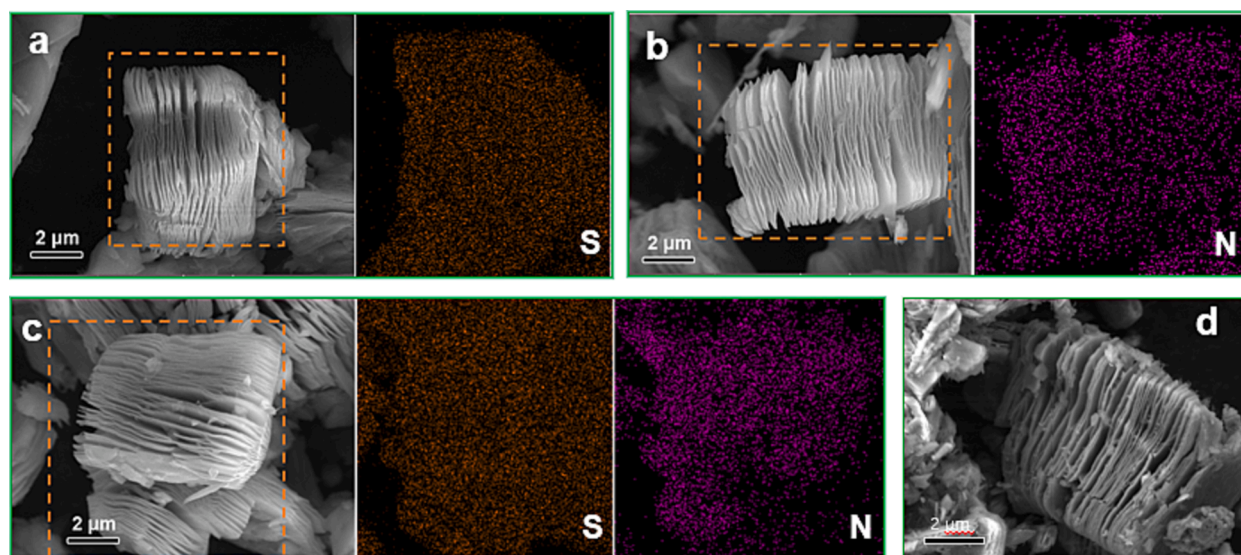


Fig. 2. SEM images and corresponding elemental maps of S-MXene (a); N-MXene (b); S/N-MXene (c); and pristine MXene (d).

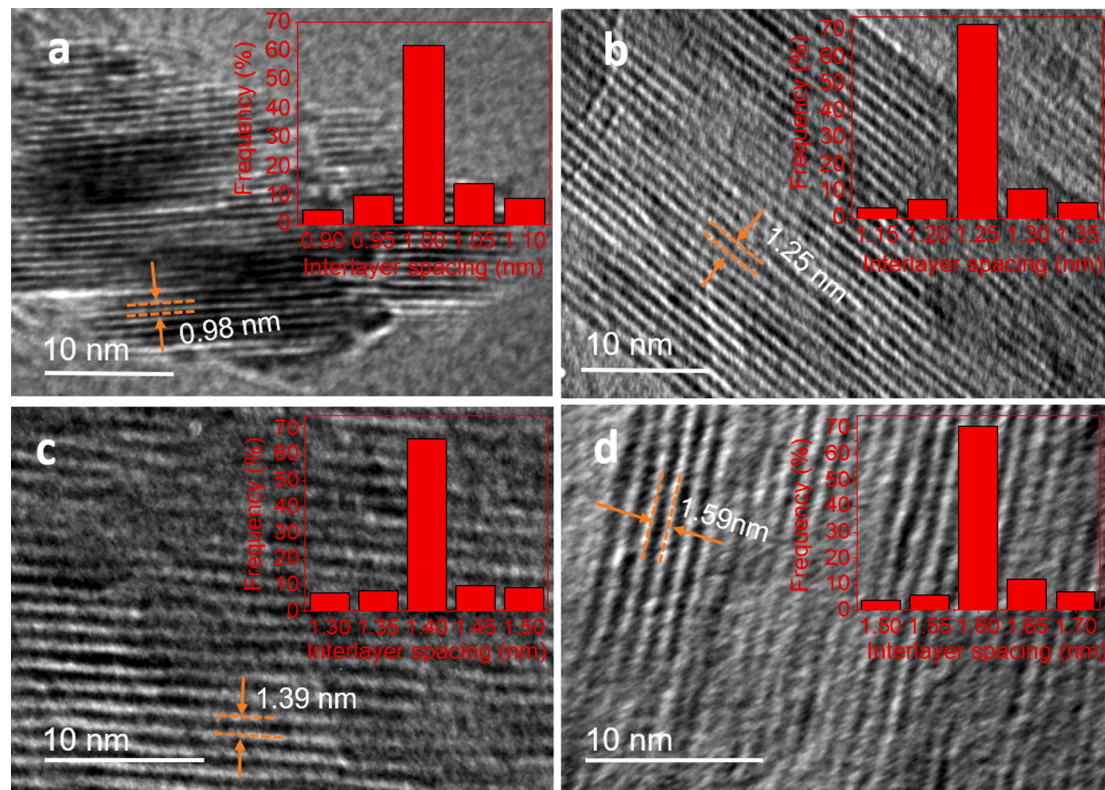


Fig. 3. HR-TEM images of pristine MXene (a), S-MXene (b), N-MXene (c) and S/N-MXene (d). The stacking of Ti_3C_2 layers is clearly visible with the mode interlayer spacing shown inset.

Package (VASP) using the general gradient approximation (GGA) Perdew-Burke-Ernzerhof functional (PBE). The van der Waals DFT-D3 correction was applied for noncovalent interactions [39–41]. A plane wave cutoff energy was set at 520 eV, and the convergence thresholds were set as 10^{-5} eV and 0.05 eV/Å for the energy and force, respectively. To avoid interactions between periodicity layers, a vacuum space between the top and bottom surfaces was fixed at 20 Å. The (001) facet of MXene was modeled with a $p(4 \times 2)$ periodic slab and five atomic layers, and the $3 \times 3 \times 1$ k-point meshes were used for the surface slabs with all atoms relaxed during optimization.

Only the interactions between the major functional groups in the interlayer, such as C-S-C and -C=S, pyridinic-N and pyrrolic-N (determined by XPS characterization, see Table S1) with Pd^{2+} were studied. Fig. S3 shows the chemical structures of the functional groups calculated by the DFT method. Specifically, C-S-C (dimethyl sulfide, DS) and -C=S (thioacetone, TA) and represent the predominant S species, and pyridinic-N the predominant N species, while 1 h-pyrrole-2-carbithioaldehyde, 5-methyl- (PCM) was included to mimic the presence of both pyrrolic-N and -C=S in S/N-MXene.

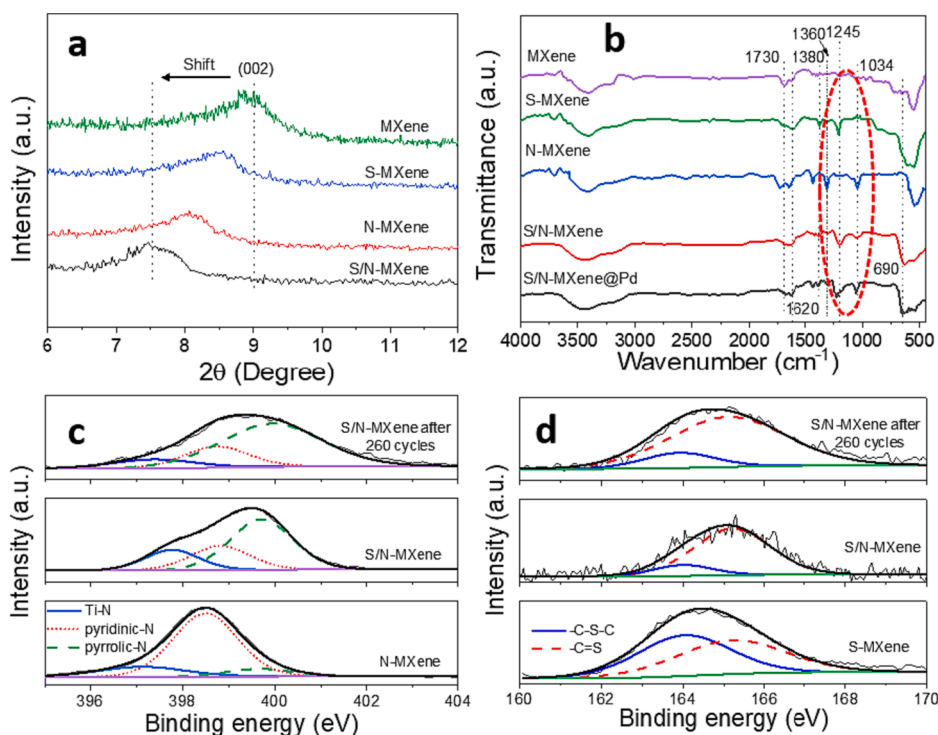


Fig. 4. XRD patterns (a); FTIR spectra (b); N 1 s core-level spectra and deconvolution of N-MXene, S/N-MXene before and after 260 cycles (c); and XPS S 2p core-level spectra and deconvolution of the S-MXene, S/N-MXene S/N-MXene before and after 260 cycles (d).

3. Results and discussion

Fig. 2 shows the SEM images of MXene and S/N-MXene materials with the corresponding EDX maps. All materials exhibited a 3D accordion-like layered structure confirming the successful exfoliation of Ti_3AlC_2 to stacks of 2D layered Ti_3C_2 via HF etching [29]. The elemental mapping (Fig. 2c) of S/N-MXene showed uniform distributions of S and N throughout the material, indicating the successful inclusion of heteroatoms. Fig. 2a and b show the EDS images of sulfur-doped MXene (S-MXene) and nitrogen-doped MXene (N-MXene) materials, again showing the good distribution of the single element.

TEM images of all prepared samples are shown in Fig. 3 and confirm that all samples exhibit the stacking of Ti_3C_2 layers [42]. The interlayer spacings of MXene, S-MXene, N-MXene and S/N-MXene were 0.98, 1.25, 1.39 and 1.59 nm, respectively, demonstrating the significant interlayer expansion of the material doped with both S and N. The observed interlayer expansion agrees with previously published studies, where phosphorous, nitrogen and sulfur doping have been shown to promote expansion of MXene interlayers by heteroatoms forming “pillars” between Ti_3C_2 layers [43,44]. The expanded interlayer spacing corresponded to an overall increase in the specific surface area (SSA) of the material, with BET isotherm SSA values of 49.5, 59.8, 66.4 and 83.2 m^2/g for MXene, S-MXene, N-MXene and S/N-MXene, respectively (Fig. S2a). The expanded interlayer and greater SSA are favorable for the recovery of target ions as the ion diffusion through the interlayer network is less hindered and the number of accessible binding sites increased. Both characteristics have been shown to lead to improved recovery capacity and kinetics [29,45].

XRD confirmed the crystalline structure of the pristine MXene and chemically doped materials, see Fig. 4a. Interlayer expansion of the chemically doped MXene is observed by the gradual shift of the (002) facet peak of MXene from 9.0° to 7.6° for the S/N-MXene. The interlayer spacings of the (002) plane of MXene, S-MXene, N-MXene and S/N-MXene were 0.91, 1.12, 1.17 and 1.33 nm, and in good agreement with the trend and values determined by HR-TEM.

Fig. 4b compares the FTIR spectra of all four materials and the S/N-

MXene sample after Pd^{2+} adsorption (to be discussed later). The peaks at 1730 cm^{-1} and 1620 cm^{-1} are characteristic of C=O and C=C [30]. For the nitrogen-doped samples, N-MXene and S/N-MXene, peaks are seen at 1034 cm^{-1} and 1360 cm^{-1} which are characteristic of C-N and Ti-N [16,46], and verify the successful doping of nitrogen into the MXene crystal structure. The C-S stretching is exclusive to the S-MXene and S/N-MXene spectra and is seen in the region of 1245 cm^{-1} and 690 cm^{-1} [30]. Furthermore, a weak peak at 1380 cm^{-1} corresponds to C=S [47]. Similar to nitrogen, these characteristic sulfur peaks confirm its successful doping into the structures of S-MXene and S/N-MXene.

XPS survey spectra revealed C 1s, Ti 2p, O 1s and F 1s peaks in all samples, while the S 2p and N 1s peaks appeared in only those samples doped by S or N, see Fig. S2b. The N 1s spectra of N-MXene and S/N-MXene (Fig. 4c) could be deconvoluted into three peaks with peak positions at 397, 398.6 and 399.9 eV that correspond to Ti-N, pyridinic-N and pyrrolic-N [11]. The pyrrolic-N content in N-MXene is 14.7% but significantly higher (55.3 at%) in S/N-MXene (Table S1).

As a highly active agent, the reaction of thiourea is highly exothermic causing the reaction temperature of the mixture (melamine + thiourea + MXene) to be 246°C and much higher than the reaction temperature of N-MXene (200°C). Previous research demonstrated an inverse relation between the reaction temperature and formation of pyridinic-N [48]. Thus, the higher reaction temperature inhibits the formation of pyridinic-N during the S/N co-doping process, contributing to the significant differences between the pyridinic-N and pyrrolic-N contents of N-MXene and S/N-MXene.

The S 2p spectra of S-MXene and S/N-MXene could be split into two peaks of -C-S-C at 164.0 eV and -C=S at 165.1 eV [30,49], see Fig. 4d. The ratio of -C=S (49.3 at%) to -C-S-C (50.7 at%) for S-MXene is about 1:1, while in S/N-MXene the -C=S content is more abundant (84.5 at%) with only 15.5 at% being -C-S-C. Interestingly, the content of S in S/N-MXene is 3.24 at%, almost double that in S-MXene (1.66 at%), indicating more S-containing species were introduced in S/N-MXene. James et al. [50] studied a series of thioaldehyde functional groups conjugated with pyrrole species, in which carbothioaldehyde ligand acts as bidentate to form various complexes. Based on this, the authors reasonably

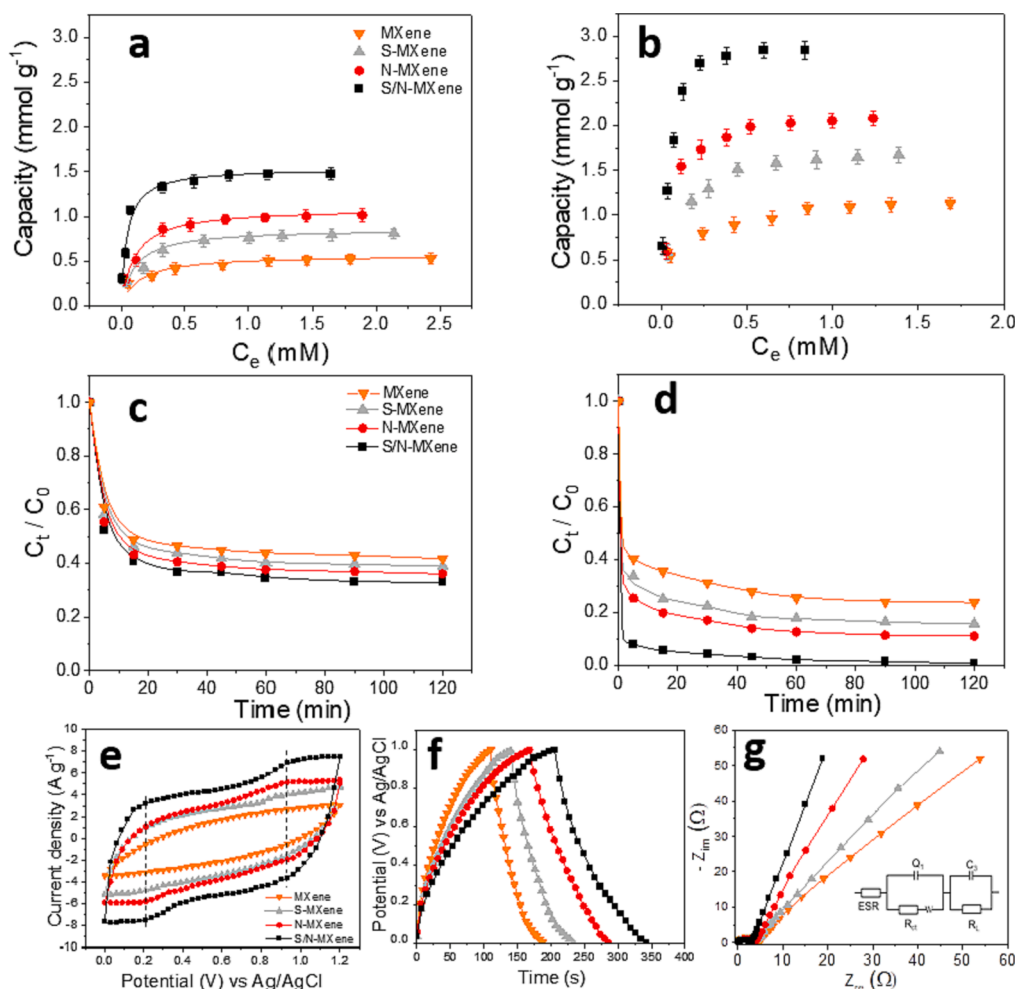


Fig. 5. Adsorption isotherms of MXene, S-MXene, N-MXene and S/N-MXene for Pd^{2+} recovery at 0 V with the Langmuir fits (a) and at 1.2 V (b); the initial concentration of Pd^{2+} was increased 0.2 to 3.0 mM at $\text{pH} = 6.0 \pm 0.1$. Adsorption kinetics at 0 V (c) and 1.2 V (d) with the corresponding PSORE fits. Cyclic voltammograms at 20 mV s^{-1} (e); galvanostatic charge/discharge at 0.5 A/g (f); and Nyquist plots (g) of the as-prepared electrodes in $0.5 \text{ mmol/L Pd}^{2+}$ solution. The circuit model shows the equivalent series resistance (ESR) with charge transfer resistance (R_{CT}) at the high-frequency region, Warburg (W) in parallel with real capacitance (Q_1), and the mass capacitance (C_3) in parallel with the leakage resistance (R_l) at the low-frequency region.

Table 1

Comparing the Pd^{2+} removal performance of S/N-MXene to other commonly studied adsorbents.

Materials	Adsorption capacity (mg/g)	Voltage (V)	Ref.
Mesoporous silica	164.2	0	[54]
MOF	226.1	0	[6]
Silica gel/graphene oxide	154.3	0	[7]
MXene	184.5	0	[29]
S/N-MXene	166.6	0	This work
	309.5	1.2	

speculate that dissociative thioaldehyde-like species generated by the decomposition of thiourea react with pyrrolic species formed by pyrolysis of melamine to produce pyrrole-carbothioaldehyde species (for the molecular structure see Fig. S3d; further discussion is given in the modeling section), thus more dissociative thioaldehyde-like species were immobilized on MXene surface to contribute higher S content and more $-\text{C}=\text{S}$ groups.

As shown in Fig. 5a, all 0 V data for Pd^{2+} adsorption could be fitted using the Langmuir isotherm with the fitting parameters summarized in Table S2. The adsorption capacity was enhanced by S or N doping and performance increased in the following order: MXene < S-MXene < N-

MXene < S/N-MXene, with the trend appearing to correspond to the changes in interlayer spacing and SSA. For S/N-MXene the maximum theoretical adsorption capacity of Pd^{2+} was 1.54 mmol g^{-1} .

The adsorption isotherms at 1.2 V are shown in Fig. 5b and trend in the same order as that seen at 0 V. However, the adsorption capacities are greatly enhanced, particularly for S/N-MXene which had the highest adsorption capacity of 2.92 mmol g^{-1} , almost double that measured at 0 V, and superior to many other adsorbent materials previously reported (Table 1). Compared to pristine MXene, which had an adsorption capacity of 1.1 mmol g^{-1} , the S-MXene capacity was 1.6 mmol g^{-1} and that of N-MXene was 2.1 mmol g^{-1} . Assuming a summative contribution to S/N-MXene, that would mean its capacity is 2.6 mmol g^{-1} , yet the actual capacity was higher at 2.9 mmol g^{-1} . This likely suggests a synergistic effect generated by S and N co-doping.

Fig. S2c shows the FTIR spectra between 1000 and 1500 cm^{-1} making visible the peaks at around 1380 cm^{-1} ($-\text{C}=\text{S}$), 1210 cm^{-1} ($-\text{C}-\text{S}$) and 1034 cm^{-1} ($-\text{C}-\text{N}$) of S/N-MXene being shifted to 1397 cm^{-1} , 1242 cm^{-1} and 1056 cm^{-1} after Pd^{2+} adsorption, indicating these functional groups are significant in the electroadsorption of Pd^{2+} . As previously reported, the S or N doping introduces abundant functional groups, such as pyrrolic-N, $-\text{C}-\text{S}-\text{C}$ and $-\text{C}=\text{S}$, which impose stronger basicity to the MXene surface for soft acid ions recovery [11,30,51]. For S and N co-doped MXene, the presence of melamine acts as the nitrogen source to generate abundant pyrrolic species which interact with dissociative

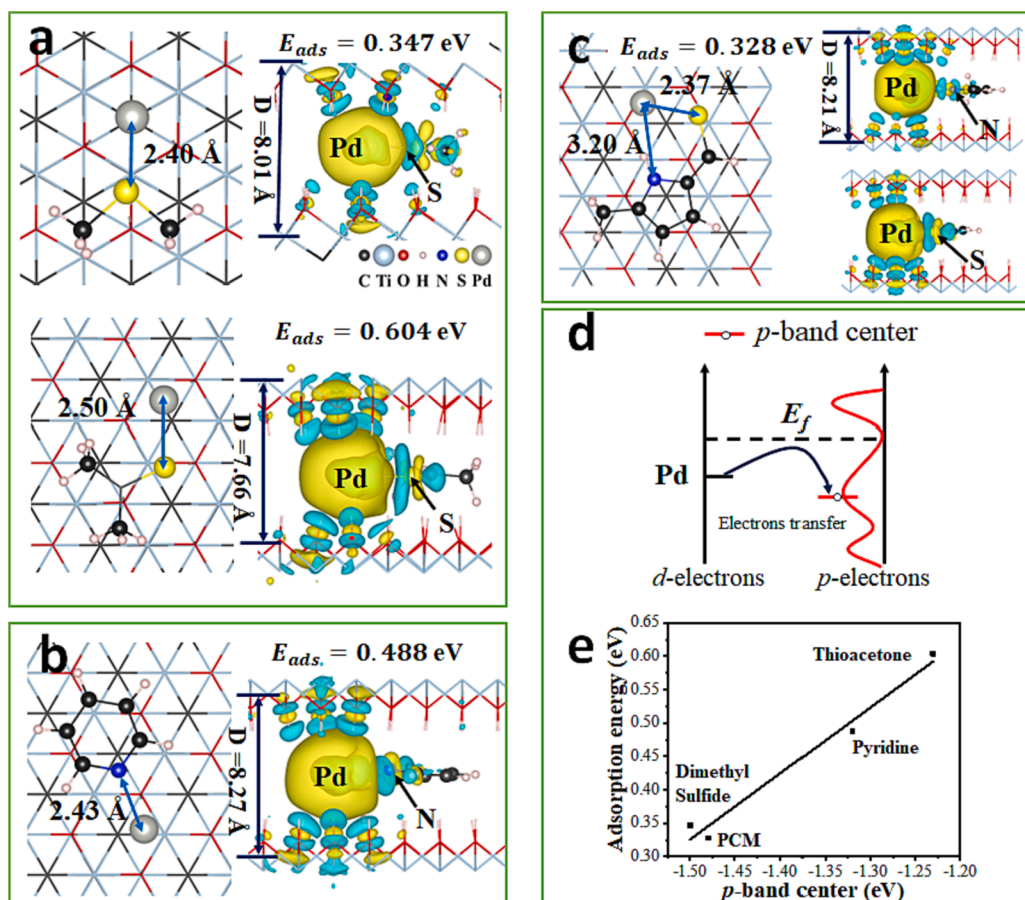


Fig. 6. Atomic structures and differential charge density analysis for MXene with (a) dimethyl sulfide (top panel) and thioacetone (bottom panel), (b) pyridine and (c) PCM. D is the interlayer spacings of MXene. (d) Schematic illustration of alignment of d -orbitals of Pd and p -orbitals of OH groups. E_f represents the Fermi level. (e) The correlation between the adsorption energy of Pd and the p -band center.

thioaldehyde-like species to form pyrrole-carbothioaldehyde functional groups, not only introducing more S-containing functional groups on MXene surface, but increasing the relative content of $-C=S$. As previously discussed, the abundant pyrrolic-N and $-C=S$ of S/N-MXene probably contribute to more charge transfer for the formation of soft-soft products [52], enhancing the adsorption capacity and selectivity for Pd^{2+} . Such synergistic effect between pyrrolic-N and $-C=S$ is further considered in the modeling section.

To better understand the interactions between S/N-MXene and the target ion, the O 1s high resolution XPS spectra of S/N-MXene before and after adsorption of Pd^{2+} are shown in Fig. S2d, and the proportions of chemical species listed in Table S1. The XPS O 1s spectra of both S/N-MXene materials can be separated into three peaks at binding energies of 529.9, 531.2 and 532.4 eV, corresponding to the chemical species of Ti-O-Ti, C-Ti-O_x and C-Ti-(OH)_x, respectively [26]. An exclusive peak at \sim 529.0 appeared in the O 1s spectrum of S/N-MXene adsorbed Pd, ascribed to the Pd-O bond [53] which accounts for 19.49 at% of the total content. Interestingly, the proportion of C-Ti-(OH)_x for S/N-MXene adsorbed Pd (12.46 at%) is significantly less than fresh S/N-MXene (28.38 at%), which the difference approximately equivalent to the content of Pd-O, demonstrating the $-OH$ groups interact with Pd^{2+} to form Pd-O bond.

All adsorption kinetics were well-fitted by PSORE with R^2 coefficients $>$ 0.99, see Fig. 5c and Table S2 for the fitted parameters. While all materials showed good adsorption kinetics, plateauing within 60 min, when applying 1.2 V the kinetics more than doubled (Fig. 5d), the slight exception being S-MXene which only doubled. The best performing material S/N-MXene had a k_2 value of $0.067 \text{ g mg}^{-1} \text{ min}^{-1}$ and removed 96.4 % Pd^{2+} within 15 min at 1.2 V. Similar to our previous

observations regarding performance, the k_2 values were higher for those materials with more expanded interlayers which facilitates enhanced ion diffusion and more accessible binding sites.

The electrochemical performance of the different materials was assessed by cyclic voltammetry (Fig. 5e), galvanostatic charge-discharge (Fig. 5f) and electrical impedance spectroscopy (Fig. 5g). For MXene, the CV curve is rectangular, albeit slightly distorted, with the shape distortion due to the charging dynamic, which is a consequence of the thick MXene electrode. When doped with single heteroatoms (S or N), the shape becomes less distorted due to the higher specific capacitance of the materials (Fig. 5e). However, weak and broad peaks in the region of 0.2 and 0.9 V were observed, which confirms that ion-binding in the heteroatom-doped materials is not purely electroadsorption, but there is a contribution from chemisorption. The effect is even more pronounced in the co-doped electrode material. Based on the GCD curves the specific capacitances of MXene, S-MXene, N-MXene and S/N-MXene are 93.4, 119.1, 142.5 and 174.5 Fg^{-1} , respectively, in good agreement with the adsorption performances seen in Fig. 5f. Fig. 5g shows the Nyquist plots for all electrodes, with the width of the semi-circle describing the charge transfer resistance which decreases in the order of MXene $>$ S-MXene $>$ N-MXene $>$ S/N-MXene. The lowest charge-transfer resistance was 3.2Ω , which can be attributed to the strong pseudo-capacitance induced by the chemical modification.

To further understand the origin of Pd selectivity, DFT calculations were performed to study the adsorption behaviors of Pd on S-MXene, N-MXene and S/N-MXene. In line with the XPS results, see Fig. 4 for details, pyridine and 1 h-pyrrole-2-carbothioaldehyde, 5-methyl-(PCM) were selected as the functional groups in the N-MXene and S/N-MXene. For the S-MXene, the two functional groups were dimethyl

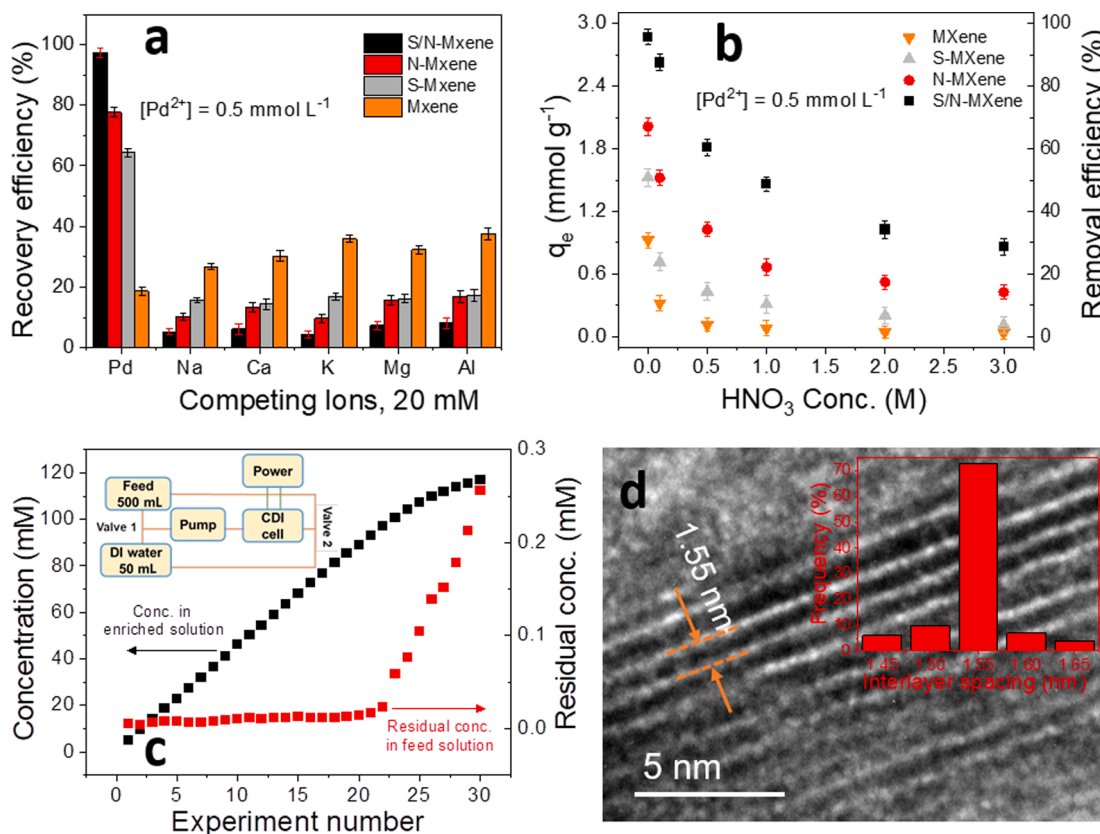


Fig. 7. Pd²⁺ recovery by all materials from a solution of competing ions (a). The Pd²⁺ concentration was fixed at 0.5 mmol/L and mixed with five competing ions each of 20 mM concentration; Influence of HNO₃ concentration on recovery capacity and efficiency of as-fabricated electrodes (b); Sequential enrichment of Pd²⁺ through step-wise adsorption (@ 1.2 V) from the test fluid and desorption (@ -1.2 V) into the enriched effluent (c). The limit for enrichment is 120 mmol/L; HR-TEM image of S/N-MXene following Pd²⁺ desorption after the 22nd cycle (d). Inset of Fig. (c) shows a block flow diagram of the CDI setup used for the enrichment tests. For Pd²⁺ recovery the feed is continuously pumped through the CDI cell before switching the feed to the enrichment stream for ion removal and regeneration of the electrode.

sulfide (DS) and thioacetone (TA) in a ratio of 50.7 % and 49.3 %, respectively. The incorporation of these functional groups into MXene resulted in interlayer spacings of 7.16–7.30, 7.64 and 7.70 Å for the S-, N- and S/N-MXene, respectively (Fig. S4). These observations are consistent with the trend observed in the TEM images (Fig. 3).

Adsorption energies of Pd (E_{ads}) were calculated using the following equation with the bulk Pd as the reference:

$$E_{ads} = E_{x-MXene+Pd} - E_{x-MXene} - E_{bulk}/n \quad (5)$$

where $E_{x-MXene+Pd}$ and $E_{x-MXene}$ are the total energies of the x-MXene (x = DS, TA, pyridine and PCM) systems with and without the adsorption of Pd. E_{bulk} is the energy of the bulk Pd with n Pd atoms in the unit cell. With this definition, a smaller value suggests stronger Pd adsorption.

As shown in Fig. 6, it is evident that Pd interacts with the functional groups N or S as well as neighboring OH groups on MXene. In the case of DS- and TA-MXene, corresponding to the S-MXene system, Pd forms bonds with S at distances of 2.40 and 2.50 Å, resulting in adsorption energies of 0.35 and 0.60 eV, respectively (Fig. 6a). For the pyridine-MXene, corresponding to the N-MXene system, Pd interacts with N resulting in an adsorption energy of 0.49 eV (Fig. 6b). In the PCM case, corresponding to the S/N-MXene system, Pd interacts with both S and N with distances of 2.37 and 3.20 Å, respectively (Fig. 6c), with an overall adsorption energy of 0.33 eV for the PCM system. Considering a fixed number of functional groups, the S/N-MXene potentially exhibits the strongest adsorption capacity, followed by N-MXene and S-MXene. This trend aligns with the experimental results. It is worth noting that although S-MXene has dimethyl sulfide functional groups that bind Pd with adsorption energies comparable to PCM, the presence of 49.3 %

thioacetone significantly impacts the adsorption capacity.

To gain a deeper understanding of the Pd adsorption trend of x-MXene, differential electron density analysis, the projected density of states (PDOS), and Bader charge analysis were performed. The results indicate that the adsorption energy difference primarily stems from the synergistic effect of OH groups and functional groups. Through the PDOS (Fig. S5), an obvious coupling between the p -orbitals of OH groups and the d -orbitals of Pd is observed. This interaction enables electron transfer from the d -orbitals of Pd to the p -orbitals of the OH groups (Fig. 6d and Table S3). However, it is important to note that the upward shift of the p -band center of the OH groups hinders electron transfer, thus weakening the binding strength of Pd. Fig. 6e illustrates the correlation between the p -band center and the adsorption energy. Thioacetone exhibits the most pronounced upward shift of the p -band center, followed by pyridine, resulting in weaker Pd binding strength. Conversely, dimethyl sulfide and PCM exhibit the most negative p -band center, leading to a strong Pd binding and the smallest adsorption energy. Overall, a downward shift of the p -band center is advantageous for Pd binding with MXene, thus enhancing Pd capacitive recovery ability. In general, the chemical hardness (the soft or hard acid) determines second-order contributions to the electron-transfer energy [52].

The effect of common ions (mono-, di- and tri-valent ions) competing against Pd²⁺ extraction is summarized in Fig. 7a. These ions were chosen as they are typically present in industrial wastewater, while Al³⁺ is found in spent Pd catalyst wastewater due to using aluminum oxide as the catalyst support [7]. The recovery of Pd²⁺ by pristine MXene was poor, less than 20 %, but following chemical doping by single and dual species, the recovery efficiency markedly increased to greater than 60 %

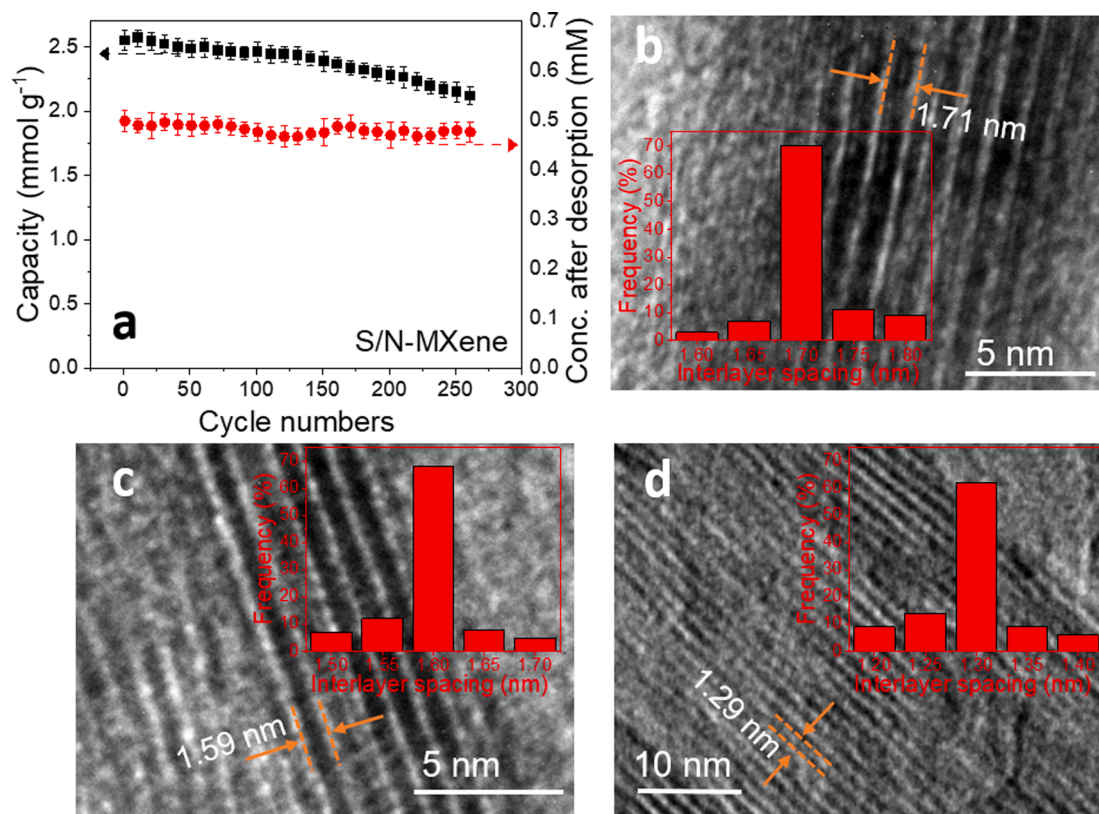


Fig. 8. Long-term cycling performance of S/N-MXene in 0.5 mmol/L Pd²⁺ solution. The black and red symbols represent the electrode capacity and solution concentration of Pd²⁺ following ion desorption from the electrode (a); HR-TEM image of S/N-MXene adsorbed Pd²⁺ after 1st cycle (b); desorbed Pd²⁺ after 1st cycle (c); and after long-term cycling – 260 cycles with Pd²⁺ desorbed (d).

and 70 % for S-MXene and N-MXene, and > 98 % for S/N-MXene. The very high recovery of Pd²⁺ by S/N-MXene demonstrates its high selectivity for Pd²⁺ over other competing ions, with recovery efficiencies of all competing ions being less than 10 %. Such selectivity is attributed to the strong and selective interaction between the soft-acid (Pd²⁺) and soft-base groups of S/N-MXene (pyrrolic-N and -C=S) [51,55].

The influence of HNO₃ concentration in the effluent on the recovery of Pd was studied (Fig. 7b). For low nitric acid concentrations (<0.1 M) the removal capacity was between 2.5 and 3.0 mmolg⁻¹, before performance gradually declined in higher nitric acid concentrations. At 3 M the removal capacity was 0.83 mmolg⁻¹. The gradual decline can be attributed to two effects: i) competition between H⁺ and Pd cationic complexes for the available binding sites; and ii) the loss of Pd cationic complexes in strongly acidic solutions. Liu et al. [34,35] published a speciation diagram for Pd(II) nitrate for increasing concentrations of nitric acid. At low nitric acid concentrations Pd is predominantly in the form of hydrated complexes of [Pd(H₂O)₄]²⁺ and [Pd(NO₃)(H₂O)₃]⁺. The neutral complex of [Pd(NO₃)(H₂O)₂] is formed with increasing nitric acid concentration, and anionic species are formed only in strongly concentrated nitric acid solutions (the fraction being less than 20 % in 3 M HNO₃). The gradual loss of cationic complexes will lower removal capacity, with the neutral complex not being removed, and anionic complexes retained on the non-working electrode that has negligible adsorption capacity.

One advantage of the CDI treatment method is the ability to repeatedly decontaminate the feed and enrich the effluent. As shown in Fig. 7c, this approach has been tested following the method previously described and shows enrichment of adsorbed Pd²⁺ into the same effluent over 22 cycles, beyond which the residual concentration in the feed increases. The increasing residual concentration signifies poor removal of ions into the enriched effluent during electrode desorption, i.e. the number of available binding sites created during electrode regeneration

is low. Based on the current test conditions, the limit for successful electro-desorption was 120 mmol/L at -1.2 V.

After 22 cycles the S/N-MXene material was imaged by HR-TEM (Fig. 7d). The mode interlayer spacing was 1.55 nm and slightly reduced compared to the pristine S/N-MXene material (D = 1.59 nm). While the change in the interlayer spacing is small, it does highlight the possibility of electrode material degradation with continuous cycling. The material robustness to continual cycling was assessed by measuring its performance until the capacity retention dropped to 80 %, which in this study was after 260 cycles, see Fig. 8a. During the first 100 cycles the capacity retention remained relatively stable and then began to gradually decline thereafter. It is noted that the solution concentration of Pd²⁺ remained unchanged during the measurement (Fig. 8a) and therefore is not a factor in the gradual loss of electrode capacity. The root cause of this capacity fade was determined from the HR-TEM images, see Fig. 8d. We have shown that for pristine-S/N-MXene the interlayer spacing is 1.59 nm, which expands to 1.71 nm (Fig. 8b) with Pd²⁺ intercalated and shrinks to 1.59 nm with Pd²⁺ desorbed (Fig. 8c). However, after 260 cycles and with Pd²⁺ desorbed, the interlayer spacing was 1.29 nm. This interlayer is significantly collapsed compared to the pristine material and is thought to result from the gradual removal of the doped functional groups from the interlayer, noting that those groups act as pillars to provide interlayer expansion relative to pristine-MXene (Fig. 3). The atomic amounts of S and N on the surface of S/N-MXene after 260 cycles were confirmed by XPS to be 2.36 at% for S and 3.37 at% for N, both lower than the fresh S/N-MXene material (3.24 at% for S and 4.46 at% for N), further demonstrating the loss of S and N containing functional groups, which is the main reason of capacity fade during long-term cycling. It is noted that the relative amounts of the different chemical species (Ti-N, Pyridinic-N, Pyrrolic-N, -C-S-C, -C=S) remained almost unchanged during prolonged cycling, see Fig. 4c and 4d, and Table S1 of the Supporting Information.

4. Conclusions

Sulfur/nitrogen co-doped MXene was successfully synthesized by facile hydrothermal method to form an electrode material for the selective recovery of Pd ions. Numerous N/S-containing functional groups were introduced to the MXene surface by S and N co-doping, with the chemical composition optimized to be preferential for Pd-ion recovery. These functional groups not only acted as pillars to expand the interlayer spacing of S/N-MXene, improving the accessibility of anchor sites and facilitating Pd²⁺ diffusion between MXene layers, but also endowed MXene with high selectivity for Pd-ion recovery via the CDI method. As a result, an excellent sorption capacity of 2.92 mmol g⁻¹ Pd²⁺ was achieved by S/N-MXene at 1.2 V, superior to most other reported materials. The sorbent showed a high recovery efficiency of 96.4 % in 15 min and satisfactory long-term cycling performance with > 80 % capacity retention after 260 cycles. S/N-MXene material showed preferential adsorption of Pd ions when mixed with other competing ions. Finally, the Pd²⁺ adsorbed on S/N-MXene could be easily enriched by reversing the applied voltage, thus stripping the adsorbed ions and avoiding the use of harsh chemical treatment. The method is shown to be efficient, environmental benign, easy to operate and economical for the practical recovery of Pd²⁺ from aqueous wastes.

CRedit authorship contribution statement

Jiming Lu: Conceptualization, Methodology, Investigation, Data curation, Formal analysis, Writing – original draft. **Shuangzhe Zhang:** Methodology, Data curation, Formal analysis, Writing – review & editing. **Chuan Zhou:** Methodology. **Xinyang Wang:** Methodology. **Binda Lu:** Methodology. **Yi Liu:** Methodology. **Yingzhi Li:** Methodology. **Timothy N. Hunter:** Methodology, Investigation, Writing – review & editing, Supervision. **Zhouguang Lu:** Methodology. **Lei Li:** Methodology, Investigation, Writing – review & editing, Supervision. **David Harbottle:** Conceptualization, Methodology, Investigation, Writing – review & editing, Supervision, Funding acquisition. **Zhenghe Xu:** Conceptualization, Methodology, Investigation, Writing – review & editing, Supervision, Funding acquisition.

Declaration of Competing Interest

The authors declare that they have no known competing financial interests or personal relationships that could have appeared to influence the work reported in this paper.

Data availability

Data will be made available on request.

Acknowledgments

The authors would like to thank financial support from several organizations including: Shenzhen Key Laboratory of Interfacial Science and Engineering of Materials (Grant No. ZDSYS20200421111401738); Leading Talents of Guangdong Province Program (Z.X.; 2016LJ06C536); Core Research Facilities, SUSTech; The Engineering and Physical Sciences Research Council (EPSRC) (D.H. and T.N.H.; EP/S032797/1); The National Natural Science Foundation of China (S.Z. and L.L.; 92270103); Guangdong basic and applied basic research foundation (L.Y.Z.; 2023A151010035). The theoretical calculations are supported by Center for Computational Science and Engineering of Southern University of Science and Technology.

Appendix A. Supplementary material

Supplementary data to this article can be found online at <https://doi.org/10.1016/j.seppur.2023.125631>.

References

- [1] F. Wu, H. Li, Y. Pan, Y. Sun, J. Pan, Bioinspired construction of magnetic nano stirring rods with radially aligned dual mesopores and intrinsic rapid adsorption of palladium, *J. Hazard. Mater.* 441 (2023), 129917, <https://doi.org/10.1016/j.jhazmat.2022.129917>.
- [2] H. Wu, S.Y. Kim, M. Miwa, S. Matsuyama, Synergistic adsorption behavior of a silica-based adsorbent toward palladium, molybdenum, and zirconium from simulated high-level liquid waste, *J. Hazard. Mater.* 411 (2021), 125136, <https://doi.org/10.1016/j.jhazmat.2021.125136>.
- [3] D.I. Kim, G. Gwak, P. Dorji, D. He, S. Phuntsho, S. Hong, H. Shon, Palladium Recovery through Membrane Capacitive Deionization from Metal Plating Wastewater, *ACS Sustain. Chem. Eng.* 6 (2017) 1692–1701, <https://doi.org/10.1021/acssuschemeng.7b02923>.
- [4] M. Zha, J. Liu, Y.-L. Wong, Z. Xu, Extraction of palladium from nuclear waste-like acidic solutions by a metal–organic framework with sulfur and alkene functions, *J. Mater. Chem. A* 3 (2015) 3928–3934, <https://doi.org/10.1039/c4ta06678b>.
- [5] Q.L. Xie, G.J. Liang, T. Lin, F. Chen, D. Wang, Selective chelating precipitation of palladium metal from electroplating wastewater using chitosan and its derivative, *Adsorpt. Sci. Technol.* 38 (2020) 113–126, <https://doi.org/10.1177/0263617420918729>.
- [6] Z. Huang, C. Wang, J. Zhao, S. Wang, Y. Zhou, L. Zhang, Adsorption behavior of Pd (II) ions from aqueous solution onto pyromellitic acid modified-UiO-66-NH₂, *Arab. J. Chem.* 13 (2020) 7007–7019, <https://doi.org/10.1016/j.arabj.2020.07.007>.
- [7] M. Li, S. Tang, Z. Zhao, X. Meng, F. Gao, S. Jiang, Y. Chen, J. Feng, C. Feng, A novel nanocomposite based silica gel/graphene oxide for the selective separation and recovery of palladium from a spent industrial catalyst, *Chem. Eng. J.* 386 (2020), 123947, <https://doi.org/10.1016/j.cej.2019.123947>.
- [8] M.R. Awual, M.M. Hasan, H. Znad, Organic–inorganic based nano-conjugate adsorbent for selective palladium(II) detection, separation and recovery, *Chem. Eng. J.* 259 (2015) 611–619, <https://doi.org/10.1016/j.cej.2014.08.028>.
- [9] J. Li, X. Wang, H. Wang, S. Wang, T. Hayat, A. Alsaedi, X. Wang, Functionalization of biomass carbonaceous aerogels and their application as electrode materials for electro-enhanced recovery of metal ions, *Environ. Sci. Nano* 4 (2017) 1114–1123, <https://doi.org/10.1039/c7en00019g>.
- [10] Y. Zhang, J. Zhou, D. Wang, R. Cao, J. Li, Performance of MXene incorporated MOF-derived carbon electrode on deionization of uranium(VI), *Chem. Eng. J.* 430 (2022), 132702, <https://doi.org/10.1016/j.cej.2021.132702>.
- [11] J. Lu, P. Kumar Mishra, T.N. Hunter, F. Yang, Z. Lu, D. Harbottle, Z., Xu, Functionalization of mesoporous carbons derived from pomelo peel as capacitive electrodes for preferential removal/recovery of copper and lead from contaminated water, *Chem. Eng. J.* (2022), 134508, <https://doi.org/10.1016/j.cej.2022.134508>.
- [12] M. Dai, L. Xia, S. Song, C. Peng, J.R. Rangel-Mendez, R. Cruz-Gaona, Electro-sorption of As(III) in aqueous solutions with activated carbon as the electrode, *Appl. Surf. Sci.* 434 (2018) 816–821, <https://doi.org/10.1016/j.apsusc.2017.10.238>.
- [13] W. Zhang, X.J. Wei, X.L. Zhang, S.L. Huo, A. Gong, X.P. Mo, K.X. Li, Well-dispersed Prussian blue analogues connected with carbon nanotubes for efficient capacitive deionization process, *Sep. Purif. Technol.* 287 (2022), <https://doi.org/10.1016/j.seppur.2022.120483>.
- [14] S. Iftikhar, M.U. Farooq, M. Sillanpää, M.B. Asif, R. Habib, Removal of Ni(II) using multi-walled carbon nanotubes electrodes: relation between operating parameters and capacitive deionization performance, *Arab. J. Sci. Eng.* 42 (2016) 235–240, <https://doi.org/10.1007/s13369-016-2301-5>.
- [15] X. Liu, J. Wang, Electro-assisted adsorption of Cs(I) and Co(II) from aqueous solution by capacitive deionization with activated carbon cloth/graphene oxide composite electrode, *Sci. Total Environ.* (2020), 141524, <https://doi.org/10.1016/j.scitotenv.2020.141524>.
- [16] P. Liu, T. Yan, J. Zhang, L. Shi, D. Zhang, Separation and recovery of heavy metal ions and salt ions from wastewater by 3D graphene-based asymmetric electrodes via capacitive deionization, *J. Mater. Chem. A* 5 (2017) 14748–14757, <https://doi.org/10.1039/c7ta03515b>.
- [17] Y. Zhang, J.Y. Wu, S.H. Zhang, N.Z. Shang, X.X. Zhao, S.M. Alshehri, T. Ahamad, Y. Yamauchi, X.T. Xu, Y. Bando, MOF-on-MOF nanoarchitectures for selectively functionalized nitrogen-doped carbon-graphitic carbon/carbon nanotubes heterostructure with high capacitive deionization performance, *Nano Energy* 97 (2022), 107146, <https://doi.org/10.1016/j.nanoen.2022.107146>.
- [18] L. Luo, Q. He, S.Q. Chen, D.X. Yang, Y. Chen, Metal-organic framework derived carbon nanoarchitectures for highly efficient flow-electrode CDI desalination, *Environ. Res.* 208 (2022), 112727, <https://doi.org/10.1016/j.envres.2022.112727>.
- [19] J.H. Feng, S. Xiong, L. Ren, Y. Wang, Atomic layer deposition of TiO₂ on carbon-nanotubes membrane for capacitive deionization removal of chromium from water, *Chin. J. Chem. Eng.* 45 (2022) 15–21, <https://doi.org/10.1016/j.cjche.2021.05.014>.
- [20] I. Ihsanullah, Potential of MXenes in water desalination: current status and perspectives, *Nano-Micro Lett.* 12 (2020) 1–20, <https://doi.org/10.1007/s40820-020-0411-9>.
- [21] B. Chen, A. Feng, R. Deng, K. Liu, Y. Yu, L. Song, MXene as a cation-selective cathode material for asymmetric capacitive deionization, *ACS Appl. Mater. Interfaces* 12 (2020) 13750–13758, <https://doi.org/10.1021/acscami.9b19684>.
- [22] P. Srimuk, F. Kaasik, B. Krüner, A. Tolosa, S. Fleischmann, N. Jäckel, M.C. Tekeli, M. Aslan, M.E. Suss, V. Presser, MXene as a novel intercalation-type pseudocapacitive cathode and anode for capacitive deionization, *J. Mater. Chem. A* 4 (2016) 18265–18271, <https://doi.org/10.1039/c6ta07833h>.

- [23] H. Khurshid, M.R.U. Mustafa, M.H. Isa, Adsorption of chromium, copper, lead and mercury ions from aqueous solution using bio and nano adsorbents: a review of recent trends in the application of AC, BC, nZVI and MXene, *Environ. Res.* 212 (2022), 113138, <https://doi.org/10.1016/j.envres.2022.113138>.
- [24] Q. Peng, J. Guo, Q. Zhang, J. Xiang, B. Liu, A. Zhou, R. Liu, Y. Tian, Unique lead adsorption behavior of activated hydroxyl group in two-dimensional titanium carbide, *J. Am. Chem. Soc.* 136 (2014) 4113–4116, <https://doi.org/10.1021/ja500506k>.
- [25] Y. Ying, Y. Liu, X. Wang, Y. Mao, W. Cao, P. Hu, X. Peng, Two-dimensional titanium carbide for efficiently reductive removal of highly toxic chromium(VI) from water, *ACS Appl. Mater. Interfaces* 7 (2015) 1795–1803, <https://doi.org/10.1021/am507472z>.
- [26] M. Rethinasabapathy, S.K. Hwang, S.M. Kang, C. Roh, Y.S. Huh, Amino-functionalized POSS nanocage-intercalated titanium carbide (Ti₃C₂T_x) MXene stacks for efficient cesium and strontium radionuclide sequestration, *J. Hazard. Mater.* 418 (2021), 126315, <https://doi.org/10.1016/j.jhazmat.2021.126315>.
- [27] M.u. Hassan, S. Lee, M.T. Mehran, F. Shahzad, S.M. Husnain, H.J. Ryu, Post-decontamination treatment of MXene after adsorbing Cs from contaminated water with the enhanced thermal stability to form a stable radioactive waste matrix, *J. Nucl. Mater.*, 543 (2021) 152566. [10.1016/j.jnucmat.2020.152566](https://doi.org/10.1016/j.jnucmat.2020.152566).
- [28] S. Wang, L. Wang, Z. Li, P. Zhang, K. Du, L. Yuan, S. Ning, Y. Wei, W. Shi, Highly efficient adsorption and immobilization of U(VI) from aqueous solution by alkalinized MXene-supported nanoscale zero-valent iron, *J. Hazard. Mater.* 408 (2021), 124949, <https://doi.org/10.1016/j.jhazmat.2020.124949>.
- [29] W. Mu, S. Du, X. Li, Q. Yu, H. Wei, Y. Yang, S. Peng, Removal of radioactive palladium based on novel 2D titanium carbides, *Chem. Eng. J.* 358 (2019) 283–290, <https://doi.org/10.1016/j.cej.2018.10.010>.
- [30] H. Tian, J. Guo, Z. Pang, M. Hu, J. He, A sulfur, nitrogen dual-doped porous graphene nanohybrid for ultrasensitive Hg(II) separation over Pb(II) and Cu(II), *Nanoscale* (2020) 16543–16555, <https://doi.org/10.1039/d0nr04558f>.
- [31] F. Rouhani, A. Morsali, Fast and selective heavy metal removal by a novel metal-organic framework designed with in-situ ligand building block fabrication bearing free nitrogen, *Chemistry* 24 (2018) 5529–5537, <https://doi.org/10.1002/chem.201706016>.
- [32] W. Wang, S. Guo, P. Zhang, J. Liu, C. Zhou, J.J. Zhou, L. Xu, F. Chen, L. Chen, Interlayer expanded MoS₂/nitrogen-doped carbon hydrangea nanoflowers assembled on nitrogen-doped three-dimensional graphene for high-performance lithium and sodium storage, *ACS Appl. Mater. Interfaces* 4 (2021) 5775–5786, <https://doi.org/10.1021/acsami.1c00609>.
- [33] G. Zou, C. Wang, H. Hou, C. Wang, X. Qiu, X. Ji, Controllable interlayer spacing of sulfur-doped graphitic carbon nanosheets for fast sodium-ion batteries, *Small* 13 (2017) 1700762, <https://doi.org/10.1002/smll.201700762>.
- [34] Y. Liu, L. Zhang, Q. Song, Z. Xu, Recovery of palladium as nanoparticles from waste multilayer ceramic capacitors by potential-controlled electrodeposition, *J. Clean. Prod.* 257 (2020), 120370, <https://doi.org/10.1016/j.jclepro.2020.120370>.
- [35] M. Jayakumar, K.A. Venkatesan, T.G. Srinivasan, P.R.V. Rao, Studies on the feasibility of electrochemical recovery of palladium from high-level liquid waste, *Electrochim. Acta* 54 (2009) 1083–1088, <https://doi.org/10.1016/j.electacta.2008.08.034>.
- [36] Q. Li, Y. Zheng, D. Xiao, T. Or, R. Gao, Z. Li, M. Feng, L. Shui, G. Zhou, X. Wang, Z. Chen, Faradaic Electrodes Open a New Era for Capacitive Deionization, *Adv. Sci.* 7 (2020) 2002213, <https://doi.org/10.1002/advs.202002213>.
- [37] C.S. Fan, S.Y.H. Liou, C.H. Hou, Capacitive deionization of arsenic-contaminated groundwater in a single-pass mode, *Chemosphere* 184 (2017) 924–931, <https://doi.org/10.1016/j.chemosphere.2017.06.068>.
- [38] O. Pastushok, F. Zhao, D.L. Ramasamy, M. Sillanpää, Nitrate removal and recovery by capacitive deionization (CDI), *Chem. Eng. J.* 375 (2019), 121943, <https://doi.org/10.1016/j.cej.2019.121943>.
- [39] C. Hao, G. Li, G. Wang, W. Chen, S. Wang, Preparation of acrylic acid modified alkalinized MXene adsorbent and study on its dye adsorption performance, *Colloid Surface A*. 632 (2022), 127730, <https://doi.org/10.1016/j.colsurfa.2021.127730>.
- [40] J. Guo, Q. Peng, H. Fu, G. Zou, Q. Zhang, Heavy-Metal Adsorption Behavior of Two-Dimensional Alkalization-Intercalated MXene by First-Principles Calculations, *J. Phys. Chem. C* 119 (2015) 20923–20930, <https://doi.org/10.1021/acs.jpcc.5b05426>.
- [41] Y. Sun, D. Jin, Y. Sun, X. Meng, Y. Gao, Y. Dall'Agnese, G. Chen, X.F. Wang, g-C₃N₄/Ti₃C₂T_x (MXenes) composite with oxidized surface groups for efficient photocatalytic hydrogen evolution, *J. Mater. Chem. A*, 6 (2018) 9124–9131. [10.1039/c8ta02706d](https://doi.org/10.1039/c8ta02706d).
- [42] M. Naguib, M. Kurtoglu, V. Presser, J. Lu, J. Niu, M. Heon, L. Hultman, Y. Gogotsi, M.W. Barsoum, Two-dimensional nanocrystals produced by exfoliation of Ti₃AlC₂, *Adv. Mater.* 23 (2011) 4248–4253, <https://doi.org/10.1002/adma.201102306>.
- [43] L. Chen, Y. Bi, Y. Jing, J. Dai, Z. Li, C. Sun, A. Meng, H. Xie, M. Hu, Phosphorus doping strategy-induced synergistic modification of interlayer structure and chemical state in Ti₃C₂T_x toward enhancing capacitance, *Molecules* 28 (2023), <https://doi.org/10.3390/molecules28134892>.
- [44] Y. Zhang, J. Li, Z. Gong, J. Xie, T. Lu, L. Pan, Nitrogen and sulfur co-doped vanadium carbide MXene for highly reversible lithium-ion storage, *J. Colloid Interface Sci.* 587 (2021) 489–498, <https://doi.org/10.1016/j.jcis.2020.12.044>.
- [45] J. Luo, W. Zhang, H. Yuan, C. Jin, L. Zhang, H. Huang, C. Liang, Y. Xia, J. Zhang, Y. Gan, X. Tao, Pillared structure design of MXene with ultralarge interlayer spacing for high-performance lithium-ion capacitors, *ACS Nano* 11 (2017) 2459–2469, <https://doi.org/10.1021/acs.nano.6b07668>.
- [46] W. Bao, L. Liu, C. Wang, S. Choi, D. Wang, G. Wang, Facile synthesis of crumpled nitrogen-doped MXene nanosheets as a new sulfur host for lithium-sulfur batteries, *Adv. Energy Mater.* 8 (2018) 1702485, <https://doi.org/10.1002/aenm.201702485>.
- [47] Y. Wei, L. Xu, K. Yang, Y. Wang, Z. Wang, Y. Kong, H. Xue, Electrodesorption of toxic heavy metal ions by mono S-or N-doped and S, N-codoped 3D graphene aerogels, *J. Electrochem. Soc.* 164 (2017) E17–E22, <https://doi.org/10.1149/2.1301702jes>.
- [48] J. Li, Z. Ren, Y. Zhou, X. Wu, X. Xu, M. Qi, W. Li, J. Bai, L. Wang, Scalable synthesis of pyrrolic N-doped graphene by atmospheric pressure chemical vapor deposition and its terahertz response, *Carbon* 62 (2013) 330–336, <https://doi.org/10.1016/j.carbon.2013.05.070>.
- [49] J. Li, Y. Zhang, X. Zhang, J. Huang, J. Han, Z. Zhang, X. Han, P. Xu, B. Song, S. N dual-doped graphene-like carbon nanosheets as efficient oxygen reduction reaction electrocatalysts, *ACS Appl. Mater. Interfaces* 9 (2017) 398–405, <https://doi.org/10.1021/acsami.6b12547>.
- [50] J.D.E.T. Wilton-Ely, P.J. Pogorzalec, S.J. Honarkhah, D.H. Reid, D.A. Tocher, Mixed-donor ligands: pyrrolicarbaldehyde and pyrroliccarbothioaldehyde σ -organyl complexes of ruthenium(II) and osmium(II), *Organometallics* 24 (2005) 2862–2874, <https://doi.org/10.1021/om050186g>.
- [51] J.H. Tang, J.C. Jin, W.A. Li, X. Zeng, W. Ma, J.L. Li, T.T. Lv, Y.C. Peng, M.L. Feng, X.Y. Huang, Highly selective cesium(I) capture under acidic conditions by a layered sulfide, *Nat. Commun.* 13 (2022) 658, <https://doi.org/10.1038/s41467-022-28217-8>.
- [52] P.W. Ayers, R.G. Parr, R.G. Pearson, Elucidating the hard/soft acid/base principle: a perspective based on half-reactions, *J. Chem. Phys.* 124 (2006), 194107, <https://doi.org/10.1063/1.2196882>.
- [53] J. Mao, S. Lin, X.J. Lu, X.H. Wu, T. Zhou, Y.S. Yun, Ion-imprinted chitosan fiber for recovery of Pd(II): Obtaining high selectivity through selective adsorption and two-step desorption, *Environ. Res.* 182 (2020), 108995, <https://doi.org/10.1016/j.envres.2019.108995>.
- [54] M.R. Awual, T. Yaita, S.A. El-Safty, H. Shiwaku, Y. Okamoto, S. Suzuki, Investigation of palladium(II) detection and recovery using ligand modified conjugate adsorbent, *Chem. Eng. J.* 222 (2013) 172–179, <https://doi.org/10.1016/j.cej.2013.02.058>.
- [55] Q. Ji, C. Hu, H. Liu, J. Qu, Development of nitrogen-doped carbon for selective metal ion capture, *Chem. Eng. J.* 350 (2018) 608–615, <https://doi.org/10.1016/j.cej.2018.06.018>.